energies

Article

Self-Starting Characteristics and Flow-Induced Rotation of Single- and Dual-Stage Vertical-Axis Wind Turbines

Muhammad Saif Ullah Khalid [1], David Wood [2] and Arman Hemmati [1,*]

[1] Department of Mechanical Engineering, University of Alberta, Edmonton, AB T6G 1H9, Canada
[2] Department of Mechanical and Manufacturing Engineering, University of Calgary, 2500 University Dr NW, Calgary, AB T2N 1N4, Canada
* Correspondence: arman.hemmati@ualberta.ca

Abstract: Despite offering promising opportunities for wind energy harvesting in urban environments, vertical axis wind turbines face limitations in terms of poor starting characteristics. In this study, we focus on analyzing improvements offered by dual-stage turbines for a range of wind velocities. Numerical simulations are performed for different phase angles between the rotors (a measure of relative angular positions of the blades in the two rotors) to quantify the response time for their starting behavior. These simulations rely on a through sliding mesh technique coupled with flow-induced rotations. We find that for $U_\infty = 4$ m/s, the phase angles of 30° and 90° substantially reduce starting time in comparison to a single-stage turbine. Dual-stage turbines with a phase angle of 90° exhibit similar or better starting behavior for other wind speeds. The phase angle of 0° in double-rotor turbines shows the poorest starting response. Moreover, it is revealed that stabilization of shear layers generated by the blades passing through the windward side of the turbine, vortex-entrapment by these rotating blades, and suppressing of flow structures in the middle of the wake enhance the capacity of VAWTs to achieve faster steady angular speed.

Keywords: wind energy; vertical axis wind turbines; wake dynamics; computational fluid dynamics

Citation: Khalid, M.S.U.; Wood, D.; Hemmati, A. Self-Starting Characteristics and Flow-Induced Rotation of Single- and Dual-Stage Vertical-Axis Wind Turbines. *Energies* **2022**, *15*, 9365. https://doi.org/10.3390/en15249365

Academic Editor: Vasily Novozhilov

Received: 3 October 2022
Accepted: 18 November 2022
Published: 10 December 2022

1. Introduction

Intensified effects of climate change and implications of greenhouse gas (GHG) emissions have recently accelerated research in the field of alternate energy systems. These resources are advantageous to existing and conventional energy harvesting and power generation technologies due to their limited GHG emissions. In this context, enormous energy can be harnessed from wind through turbines in urban and off-shore environments for power generation. To this effect, horizontal-axis wind turbines (HAWTs) have gained popularity due to their capacity for greater power generation. However, vertical axis wind turbines (VAWTs) provide more promising alternatives in urban environments due to their small size and better aerodynamic performance at lower wind speeds. VAWTs are quieter and their omnidirectional performance is suited to high turbulence levels in the urban setting. There are some design concerns over the performance of these turbines that require further research. Mainly, Darrieus-type or straight-bladed VAWTs require a faster self-starting mechanism that does not rely on any external support or excitation. There exist several definitions in the literature for defining the self-starting phenomenon in VAWTs [1–4]. For a horizontal-axis turbine, Ebert and Wood [5] suggested that it was simply necessary to minimize the time taken for blades to reach a reasonable rotational speed to start loading the generator in order to produce power. According to Kirke [1], a turbine must generate significant power for the self-starting process to commence adequately. Lunt [2] defined this process for a turbine when it accelerates from a stationary position to produce usable power output. Moreover, Takao et al. [3] presented a more appropriate definition for a self-starting turbine without involving vague terms, such as usable outputs or significant power. They defined a turbine as self-starting if it accelerated from a static state and attains a steady-state speed that is greater than the wind velocity. It means that a turbine should have tip-speed ratio more than one to complete the self-starting process. Usually, improvements in designs of VAWTs to address this particular issue drastically impact their power production [6]. Hence, novel techniques are needed for VAWTs to enhance their self-starting process adequately towards a desired power outcome.

In the literature, various efforts were reported to analyze and hasten the self-starting of VAWTs. For example, Dominy et al. [7] developed a numerical model with symmetric NACA-0012 blade profiles to demonstrate that a three-bladed turbine always had a potential to self-start under steady wind flow. Their work also showed that the self-starting process of a two-bladed VAWT depended on the initial orientations of the blades. Later, a theoretical framework was developed by [8] using momentum models, and experiments were also performed to examine the effects of airfoil shape on a vertical axis rotor. Such momentum-based models were also used to determine virtual camber in VAWTs to correctly predict their power on very low tip-speed ratios [9]. Worasinchai et al. [10] explained similarities in the aerodynamics of flapping wings and VAWTs. They suggested that utilizing unsteadiness in the upstream wind by the rotor geometry could enhance thrust generation by the blades. They also concluded that this exploitation of unsteadiness was essential for the VAWT to self-start, because the turbine was locked in a certain "dead" regime when thrust was not continuously generated by the blades. To this effect, many studies [11–14] have recently focused on modifying blade profiles and turbine geometries to increase the starting time of VAWTs. Sun et al. [15] examined the effects of symmetric and asymmetric cross sections of blades and their inertial properties on the self-starting capacity of VAWTs. They reported that variations in the geometry of turbine blades could help enhance the strength of the initially formed vortex in terms of vorticity and size over a blade's surface to reduce the starting time. Based on this finding, blades with EN0005-based cross-sectional profiles showed better self-starting characteristics. However, they also observed that other asymmetric blade profiles (e.g., NACA-1425 or NACA-4425) with selected camber and thicker symmetric profiles (e.g., DU06-W-200) showed superior power production at wind speeds below 6 m/s. Moreover, blades with thinner cross sections generated more power at higher wind speeds. Celik et al. [6] performed numerical simulations to examine how the number of blades and moment-of-inertia impact the self-starting of H-type straight-bladed VAWTs. Their findings indicated that this process remained insensitive to inertial characteristics of the blades. Another important observation in their work involved reducing the starting time of a turbine by increasing the number of blades, which resulted in reduced power output. More recently, Sun et al. [16] also studied the impact of variations in the number of blades and offsets in their pitching angle on the power output. Their findings revealed that an optimum pitching angle of -4° significantly increased the power output as well as minimized the time for a turbine to self-start at wind speeds over 9 m/s. A very recent work by [17] presented an interesting approach to compute localized flow speeds near blades and their dependence on tip-speed ratios of VAWTs during different revolutions when they are self-starting. They concluded that drag force along with lift could be a substantial contributor in driving these turbines initially when the blades would be likely to experience high angles-of-attack.

Another very promising modification in designs of VAWTs involves the addition of another rotor inside the primary rotor of H-type VAWTs. A few studies have reported the benefits of increase in power generation and improved static torque by such configurations [18–28]. Particularly, Torabi Asr et al. [21] performed two-dimensional numerical simulations to show faster starting and more power extraction of double-stage VAWTs than a single-rotor counterpart by offering smaller cut-in wind speeds and lower starting time. Later, Chen et al. [29] employed computational simulations to investigate the role of distance between the two rotors for the aerodynamics and starting of dual-stage VAWTs. In their cases, these turbines produced less power compared to a single-rotor configuration, but significantly reduced the starting time. With this background, it is important to further analyze effects of the phase angle between rotors of dual-stage turbines for a range of wind speeds to identify adequate locking mechanisms under distinct flow conditions to attain the desired results. Another motivation for choosing such configurations for aerodynamic designs comes from schooling behavior of fish, which can move in circular formations. It demonstrates prospects to enhance performance metrics as also recently shown by [30] for a Savonius turbine. More nature-inspired mechanisms to improve energy harvesting from VAWTs were described by [31]. Hence, we focus on this particular subject in our present work and employ computational simulations to quantify the performance of both single- and dual-stage turbines and qualitatively analyze their self-starting behavior and power generation capacity. The primary novelty of our present work lies in explaining physical mechanisms around the rotating blades in VAWTs, which play a critical role in quickly reaching steady-state. Another aspect is explaining the impact of different geometric configurations on their self-starting behavior. The simulations were made without loading the rotor because any load would increase the starting time. It is emphasized that the simulations do not give information on the power extraction capacity of dual-rotor VAWTs. This is an important topic, but one that should be explored only if the dual-rotor turbine starts more rapidly than a single-stage one.

The manuscript is organized as follows. Section 2 explains the geometric and kinematic configurations of vertical axis wind turbines as well as our numerical methodology for flow-induced rotations of vertical axis wind turbines. It also presents detailed validations and verification of our computational strategy. In section sec:esults, we first elucidate the quantitative performance metrics of the single- and dual-rotors VAWTs supplemented later by the governing unsteady physical mechanisms that lead the turbines to their steady-state rotations.

2. Numerical Methodology

In this section, we describe the computational methodology employed to perform simulations for single-stage and dual-stage VAWTs. This analysis includes simulating their flow-induced rotation at various operating conditions. We also provide details on the verification and validation studies associated with the current setup.

2.1. Geometry and Kinematics

Two-dimensional single-stage and dual-stage configurations of H-type Darrieus vertical axis wind turbines with rigid symmetric NACA0018 airfoils were employed for this study. It is important to note that the flow-induced motion of the rotors in the present work does not include structural deformations of the blades. Schematics of the single- and double-rotor configurations of the VAWTs presently under consideration and a schematic of the flow domain are shown in Figures 1 and 2, respectively. The key details about kinematics and geometries are outlined in Table 1 along with the ranges of governing parameters that quantify the performance of VAWTs.

Table 1. Geometric and flow parameters for VAWTs, where subscript “1” denotes the primary, outer rotor and “2” the inner, secondary one.

Parameters	Value
Cross section of blades	NACA0018
No. of blades in single-stage turbines	3
No. of blades in dual-stage turbines	6
Free-stream velocity (U_∞)	4–10 m/s
Chord length of blades in primary rotors (c_1)	0.06 m
Radius of the primary (outer) rotor (R_1)	0.5 m
Ratios of radii for primary and secondary (inner) rotors	$R_1/R_2 = 0.85$
Geometric ratios for blades in primary and secondary rotors	$c_1/D_1 = c_2/D_2 = 0.06$
Angle between the blades of primary and secondary rotors (ϕ)	0°–90°
Reference area (A)	1 m^2

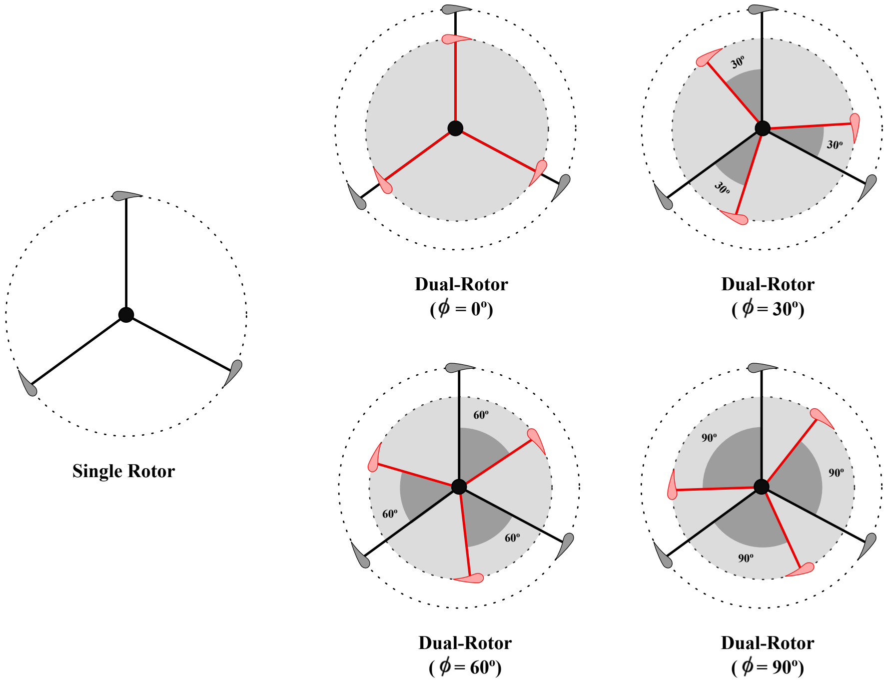

Figure 1. Schematics of single- and dual-stage turbines.

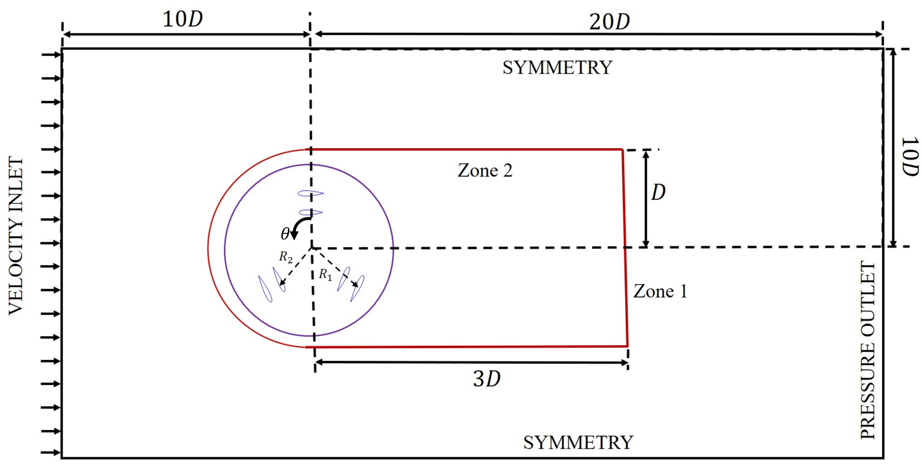

Figure 2. A schematic (not to scale) of the computational domain with the description of boundary conditions.

2.2. Flow Solver

The simulations were performed using ANSYS Fluent 2020R2 [32], a commercial finite-volume based computational solver, which has gained popularity among researchers for simulations of flow over wind turbines [33–36]. Here, incompressible continuity and unsteady Reynolds-averaged Navier–Stokes (URANS) equations are solved in Cartesian coordinates through the pressure-based algorithm. Although a PISO (pressure implicit with splitting operators) scheme is recommended for unsteady flows [37], it is usually advantageous when a large time step (Δt) was adopted to computationally march in time. Hence, the Semi-Implicit Method for Pressure Linked Equation (SIMPLE) algorithm is adopted for our current simulations to improve the computational efficiency.

The least square cell-based technique was utilized for the computation of gradient terms, second-order scheme for convective pressure terms, and second-order upwind technique for diffusion terms in the momentum equation. Although third-order algorithms may also be used for the terms with Laplacian operator, those are computationally expensive. The advantage of upwind schemes is the provision of greater stability in numerical simulations. The unsteady term was numerically approximated by the second-order implicit scheme, as also recommended by [38]. These unsteady simulations were performed through the sliding-mesh technique, which allows physical rotation of the turbine without disturbing the original mesh. Rezaeiha et al. [39] suggested that Shear Stress Transport (SST) turbulence models performed well in capturing the flow features for VAWTs and results obtained through them closely matched with experiments. Therefore, a four-equation transition SST turbulence model was employed to predict the turbulent flow features and accurately capture the laminar-to-turbulence transition. The convergence criterion for the iterative solution at each time step was set to 10^{-4}. All the simulations ran for sufficient time, so that the VAWTs attain their steady-state tip-speed ratios.

2.3. Computational Domain and Boundary Conditions

An H-grid method with a rectangular computational domain was used in this study, shown in Figure 2. A uniform flow-velocity was prescribed at the inlet boundary located at a distance of $10D$ from the central axis of the turbine. Gauge pressure was set as zero on the pressure outlet boundary located $20D$ away from this axis. Top and bottom boundaries were set as symmetry, and each one was located at a distance of $10D$ from the center of the turbine. All domain boundaries were adjusted following the recommendations of Rezaeiha et al. [40]. The main objective of performing sensitivity studies on domain-size independence is to ensure accuracy in capturing the physical phenomena around rotating blades and computing their performance parameters. Rezaeiha et al. [40] concluded through extensive $2D$ and $2.5D$ simulations that inlet, outlet, and side boundaries should be kept at a minimum distance of $10D$ from the center of the turbine to minimize their impact on numerical accuracy, let the wake fully resolve, and avoid blockage effects.

To incorporate the sliding mesh techniques, the computational domain was divided into three zones for both single- and dual-stage VAWTs. Zones 1 and 2 are shown in Figure 3. Both these zones remain stationary and are connected by an interface, which enabled communication of flow information between neighboring domains through a non-conformal meshing algorithm. Zone 2 was used to capture complex details of the wake of the rotating turbine. Figure 3a presents the meshing features inside all three zones. Here, Zone 3 contains blades for the outer and inner stages of the turbine. This domain rotates around the central axis of the VAWT. Figure 3b,c exhibit the very fine grid near the leading and trailing edges of the foils with $y^+ = 1$, respectively, which is sufficient to accurately capture the boundary layers around these rotating structures. It is evident from Figure 3d that we control these mesh settings in order to slowly vary the mesh size and avoid large gradients. Numerical errors are avoided by keeping the same cell size around the interface boundary between the rotating and static domains. The current setup follows the recommendations of Rezaeiha et al. [40], whose study reveals that the radius of a rotating domain in such simulations does not have significant effects on the aerodynamics of wind turbines. Although the Reynolds number Re for flows around a rotating machinery involves velocity scales that are dependent on both free-stream/local air speed and the angular velocity of the machines, the *"averaged" Re can be defined as:*

$$\mathrm{Re} = \frac{({U_\infty}^2 + \Omega^2)^{0.5} D_1}{\nu} \tag{1}$$

where Ω denotes the angular speed of the turbine, and ν is the kinematic viscosity of air. Considering the speeds of air in this work, the initial values of Re range from 2.7×10^5 to 6.75×10^5. As a turbine accelerates to gain its steady rotational speed, Re increases substantially.

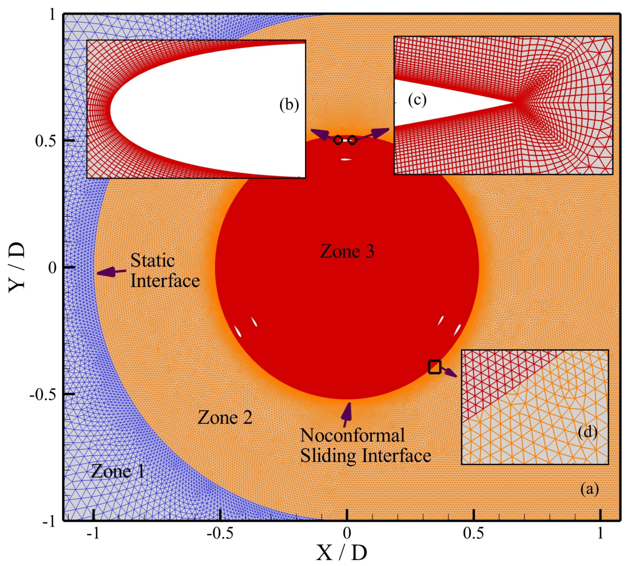

Figure 3. Mesh settings in difference zones of the flow domain and near the blades.

2.4. Flow-Induced Rotation of Turbines

The simulations for flow-induced rotation of single-stage and dual-stage VAWTs provide insights to their self-starting with different geometric configurations. In such cases, turbines are allowed to rotate passively as a result of flow-induced forces and moments on blades instead of prescribing the angular velocity of rotors. For this purpose, the six degrees-of-freedom (6DoF) solver in ANSYS Fluent [32] was employed to solve the following equation for dynamics of the rotational structure.

$$I\ddot{\theta} = \sum M_{\circ} \tag{2}$$

where I represents the moment of inertia of the VAWT, $\ddot{\theta}$ denotes its angular acceleration, and $M_{\circ}$ is the total moment produced by the blades of the turbines around the central axis, which makes it equal to τ. Next, the angular velocity ($\Omega = \dot{\theta}$) of the turbine is computed by numerically integrating Equation (2) through a trapezoidal rule. It is important to mention that coupled rotation of the two rotors for dual-stage turbines is considered in the present study, where both outer and inner rotors rotate have the same angular velocity. Here, the summation of aerodynamic moments represents the total torque induced by the wind on rotors. The mass of each blade in the outer and inner rotors is considered as 0.06 kg and 0.051 kg, respectively. Their respective moments-of-inertia are then computed as:

$$\begin{aligned} I_{outer} &= 3m_1{R_1}^2 \\ I_{inner} &= 3m_2{R_2}^2 \end{aligned} \tag{3}$$

where m_1 and m_2 show masses of each blade in the outer and inner stages, respectively. Hence, the single- and dual-stage turbines have $I = 0.045$ kgm^2 and 0.0726 kgm^2, respectively. It is important to note that the values of masses for blades in these turbines are chosen to keep moments-of-inertia in the range of those provided by others in the literature [6].

2.5. Key Performance Parameters

The following parameters are generally used to describe the flow as well as the geometric and kinematic features of wind turbines. First is the tip-speed ratio defined as:

$$\lambda = \frac{\Omega R_1}{U_\infty} \tag{4}$$

where R_1 is the radius of the outer rotor of a turbine, and U_∞ represents the free-stream flow velocity.

In order to measure the aerodynamic performance of wind turbines, non-dimensional torque (moment) and power coefficients, denoted as C_m and C_P, respectively, are computed for all cases, which are defined as:

$$C_m = \frac{\tau}{qR_1 A}, \quad C_P = \frac{\tau\Omega}{qU_\infty A} \tag{5}$$

where τ denotes torque of the VAWT, A is the swept area of the turbine, and $q = \rho U^2{}_\infty/2$ is the dynamic pressure. The swept area is a factor computed through multiplying the turbine height (1 m for the current 2D cases) with its outer diameter.

2.6. Validation and Verification

The accuracy of computational results depends on mesh topology, which also has a strong impact on boundary layer flows. Hence, we performed detailed grid convergence tests to ensure that the results were not significantly impacted by an increase in mesh sizes. For this purpose, the computational domain around a dual-stage VAWT was decomposed in non-homogeneous grids with unstructured triangular cells in the fluid domain and 26 layers of quadrilateral elements around each blade to accurately resolve boundary layers. We controlled the grid size by changing the maximum sizes of the grid in different zones while keeping y^+ value of the order of 1. This parameter helps compute the height of the first cell from the blade's surface. Its accuracy plays a critical part in resolving the viscous sublayer in turbulent boundary layers. Here, three mesh sizes were considered for a constant tip-speed-ratio of $\lambda = 4.0$, the details of which are provided in Table 2. In these simulations, we set the time-step size according to a change of 0.2° in the azimuthal angle per time step. The maximum cell size for the outermost static domain, identified as Zone 1 in Figure 3 is 0.5 for all the cases considered here, because the far-wake region does not influence the dynamics of turbine significantly.

Table 2. Details of mesh topology in different zones for grid-independence tests, where the sizes are nondimensionalized by the outer diameter (2R1) of the VAWTs

Details of Grid	G1 Coarse	G2 Medium	G3 Fine
Mesh Nodes on Each Blade	400	400	400
Maximum Size in Zone 2	0.02	0.015	0.01
Maximum Size in Zone 3	0.002	0.00135	0.001
Total Number of Cells	271,223	510,530	1,199,418

Figure 4 presents profiles of moment coefficient of one outer blade in a dual-stage rotor, undergoing rotation with $\lambda = 4.0$. It is apparent that all three grids produce the same C_m, and small differences arose only for $240° < \theta < 350°$. Because the grid configuration G_2 matches more closely to G_3, the remaining simulations were run with the mesh settings of G_2. In order to further demonstrate the effectiveness of our grid-convergence study, we employed another parameter called the determination coefficient (R^2) and used by [17,41] to quantify variations in the final solution for different grids. The expression is,

$$R^2 = 1 - \frac{\sum_{\theta=0^\circ}^{360^\circ}[C_m(\theta) - C_{m,final}(\theta)]^2}{\sum_{\theta=0^\circ}^{360^\circ}[C_m(\theta) - C_{m,average}]^2} \tag{6}$$

where $C_m(\theta)$ and $C_{m,average}$ are the instantaneous and cycle-averaged moment coefficients for the grid under consideration, In addition, $C_{m,final}(\theta)$ is the moment coefficient for the finest mesh. This determination coefficient takes values of 0.9829, 0.9844, and 1 for the coarse, medium, and finest grids, respectively, in the present study.

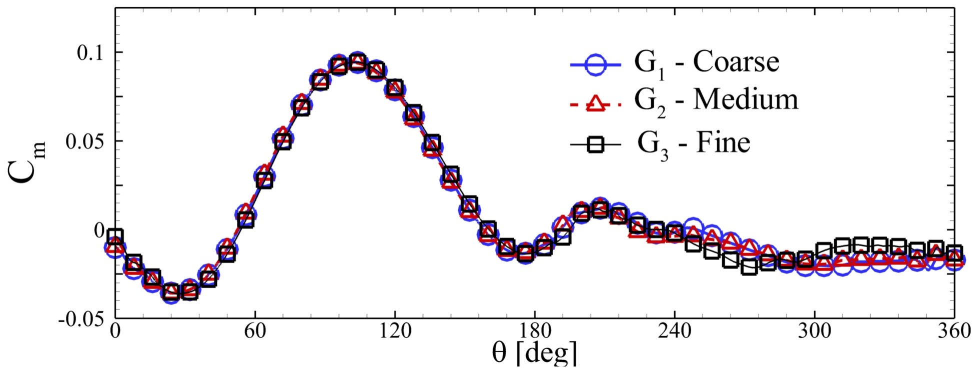

Figure 4. C_m of a single blade in a dual-stage turbine ($\phi = 0°$) rotating with $\lambda = 4.0$ for different grid configurations.

The rotation of blades in close vicinity could influence flow separation from their surfaces. There are two important aspects for modeling such phenomena: (i) fine resolution of mesh in the vicinity of the rotating blades so that unsteadiness and important length scales of flow features may be well captured and (ii) accurate modeling of turbulent flows around the blades, which may be subjected to transitional effects. Figure 3 shows the fine resolution of mesh in the regions between and around the blades. As demonstrated by [40], SST-based models provide the best agreements with experimental results for flow features around blades in VAWTs. These features include dynamic stall along with the related growth, shedding, and traversing of vortices in the wake. The four-equation transition SST model proves to be a superior choice to predict circulation and timings of vortex shedding process from the rotating blades.

We validate our computational setup using previously published experimental [42] and numerical studies [15,43]. The specifications of the VAWT for the validation study are: NACA0018 represents the cross section of a blade with chord-length of 0.083 m, the radius of the rotor in this case is 0.375 m, moment-of-inertia of the turbine is 0.018 kgm^2, and the wind speed is 6 m/s. Figure 5 shows variations in tip-speed ratios of a vertical axis wind turbine, where the present simulation methodology performs better in comparison to the previously reported numerical investigations with respect to experiments of Rainbird [42]. Here, T denotes the time when the turbine attains its steady-state tip-speed ratio. When the turbine begins its rotation, it undergoes a slow acceleration stage up to $t/T = 0.7$, after which a rapid increase in its rotational velocity is observed.

Rainbird [42] reported the steady-state tip-speed ratio of $\sim$3.40. Asr et al. [43] and Sun et al. [15] found this value to be 4.3 and 3.63, respectively. The present methodology not only predicts the rotation rate during the acceleration stages with comparative accuracy, but also gives the final value of the tip-speed ratio as 3.70, which is close to the one determined experimentally. It is important to mention that Asr et al. [43] and Sun et al. [15] employed first-order implicit time-marching numerical schemes in their studies, which could cause overprediction of performance parameters for the VAWT. A plausible reason for more accurately capturing the temporal variations in the angular velocity in our simulation is the utilization of the second-order implicit algorithm to march in time. Using the sliding-mesh technique may also help achieve better results because dynamic meshing techniques introduce additional diffusion and constant variations in the grid quality. The reason for a slight overprediction of the steady-state λ is the two-dimensional modeling of this VAWT. The span of each blade in the experiments of Rainbird [42] was 0.60 m. This feature introduces span-wise flow over a blade and consequent reduction in aerodynamic torque. Nevertheless, our two-dimensional simulations capture the relevant quantitative and qualitative details with reasonable accuracy. The time-step size (dt) used for these simulations is 0.0005 s, which is sufficiently small to capture highly unsteady flow characteristics around the turbines, and it is also consistent with the recommendations of [43].

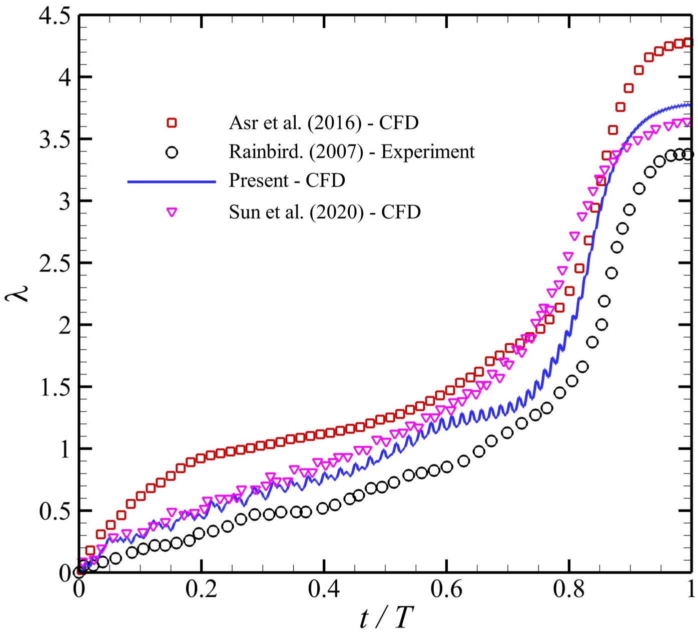

Figure 5. Results to validate the present computational methodology using experimental and numerical results from literature [15,42,43].

3. Results and Discussion

In this section, we discuss effects of the wind velocity on self-starting characteristics and passive rotation of VAWTs. In this context, the performance of single-stage and dual-stage VAWTs are compared in detail. To explore the dynamic response of multi-stage turbines, the phase angle between inner and outer rotors is varied from 0° to 90°.

There are different perspectives within the wind turbine community on the definition of the self-starting process of VAWTs [7,10,44], as well as how best to illustrate it. Generally, a turbine is considered as self-starting if it can accelerate and attain a steady-state angular velocity in response to the aerodynamic forces and moments on its own without any external excitation [8,15]. Its ability to self-start can be determined through the time taken to reach a steady-state rotational speed. Figure 6 shows variations in λ versus time, non-dimensionalized by the factor U_∞/R_1 for single- and dual-stage turbines. For the lowest wind speed, i.e., $U_\infty = 4$ m/s in Figure 6a, the dual-stage turbines are observed to reach steady-state λ more quickly compared to their single-stage counterpart. Here, time is nondimensionalized by U_∞/R_1, and it is denoted with the symbol $t^\star$. The single-stage VAWT experiences slow acceleration until $t^\star = 80$ from which point onward it rapidly increases its rotation rate and attains the steady-state condition of $\lambda = 5.06$ at $t^\star = 114$. It is interesting to notice that the dual-stage VAWT with $\phi = 0°$ cannot attain high λ even after rotating for a longer period of time. Its maximum λ remains at 0.63, which is achieved at $t^\star = 100$. Its dynamic response seems to become locked in a state, which is unrecoverable, and the underlying reasons are unclear. This kind of behavior was previously observed by Liu et al. [44] for a vertical axis tidal turbine, and they termed it as the "*unstable equilibrium mode*". For $\phi = 30°$ and 90°, the dual-stage turbine accelerates more quickly compared to the single-rotor VAWT. The dual-stage versions, except for the case of $\phi = 0°$, attain steady-state $\lambda = 3.83$. However, the turbine with $\phi = 30°$ reaches its steady-state condition faster than the other cases. Hence, dual-stage turbines outperform the one with a single rotor at very low wind speeds in terms of better self-starting characteristics.

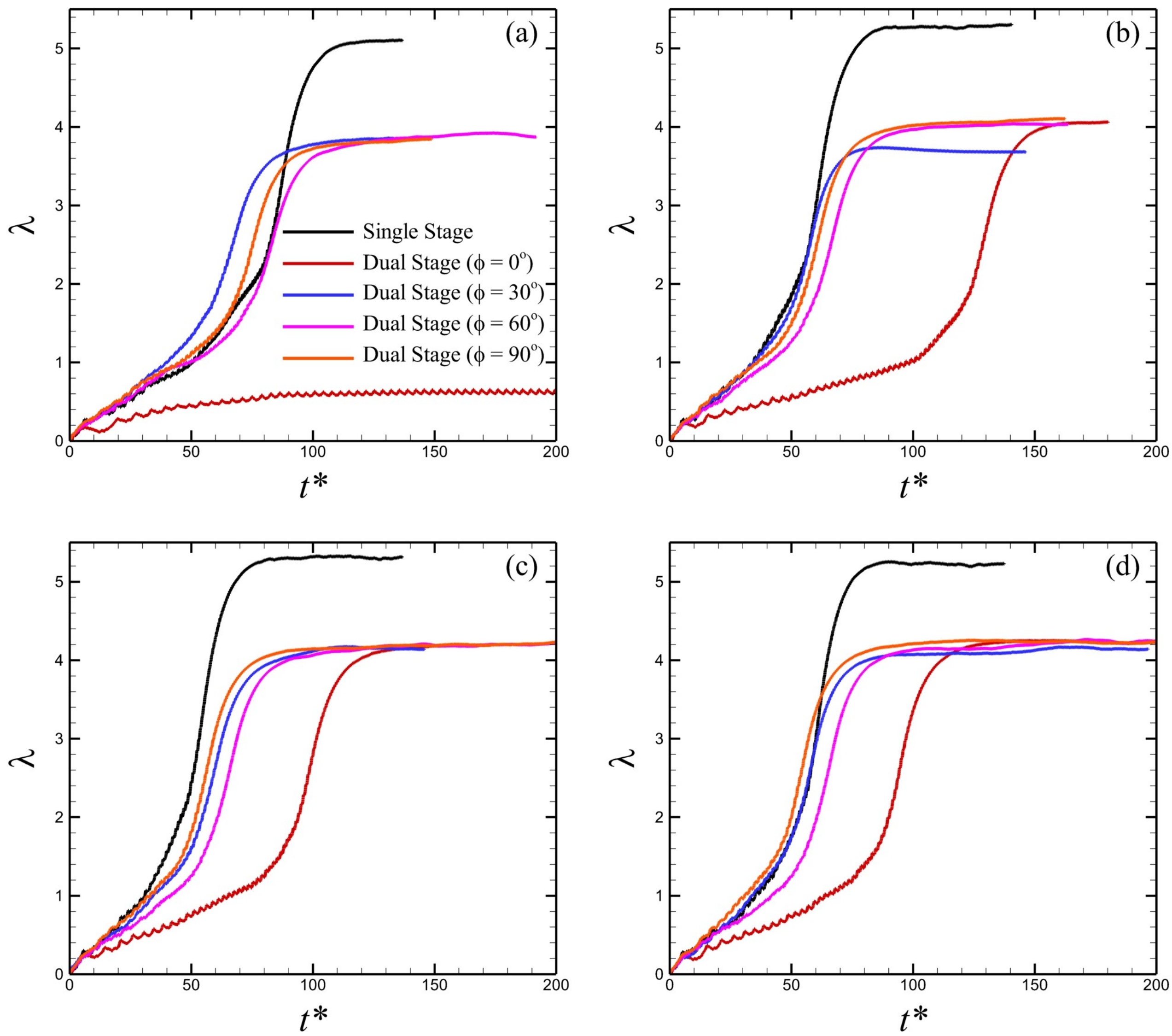

Figure 6. Temporal variations in tip-speed ratios (λ versus nondimensional time t^*) of single- and dual-stage turbines for $U_\infty =$ (**a**) 4.0; (**b**) 6.0; (**c**) 8.0; and (**d**) 10.0 m/s.

For the case of a higher wind speed at $U_\infty = 6.0$ m/s, the single-stage VAWT accelerates very rapidly and achieves $\lambda = 5.26$ at $t^\star = 88.6$. Performance of the dual-rotor VAWT with $\phi = 0^\circ$ remains the lowest of all configurations. Although it attains the same steady-state condition with $\lambda = 4.04$, as was observed for turbines with $\phi = 60^\circ$ and 90°, it takes more time. The configuration with $\phi = 30^\circ$ is the fastest amongst the configurations considered here; however, it achieves the maximum λ of 3.7. As shown in Figure 6c, the self-starting capability of the single-stage VAWT is superior to that of other dual-stage turbines at $U_\infty = 8.0$ m/s. The VAWTs with two rotors spend more time to reach their steady-state with $\lambda = 4.15$, whereas those with $\phi = 30^\circ$, 60°, and 90° take $t^\star = 107$, 115, and 95 to reach steady-state, respectively. Looking at the trends of λ for $U_\infty = 10$ m/s in Figure 6d, it can be assessed that $\phi = 30^\circ$ or 90° is advantageous for dual-stage VAWTs. In addition, a reasonable argument for the rapidly accelerating single-stage turbine at higher wind speed is related to its lower moment-of-inertia. It is evident that the multi-rotor VAWTs with phase angles between 30° and 90° offer more promising self-starting characteristics even with 38% greater inertia. Simultaneously, configurations with $\phi = 0^\circ$ should be avoided.

In order to have more insight into the aerodynamic performances of these turbines, the total torque experienced by the single-stage turbine and four different configurations of dual-rotor VAWTs are plotted in Figure 7. Here, all turbines initially experience small torque with more intense random fluctuations. Nevertheless, all the cases exhibit the production of positive time-averaged τ, which enhances acceleration of turbines. As time progresses, these rotating structures, except the one with $\phi = 0°$, experience sharp increments in their torque profiles, which we call the "overshoot" phenomenon. After passing through this stage, the single-stage turbine and dual-rotor VAWTs with $\phi = 30°$, $60°$, and $90°$ reach their periodic steady-state response in terms of aerodynamic torque. After attaining their steady-state operations stages, all turbines produce zero time-averaged torque, which reflects the attainment of steady angular speed. Although the dual-stage VAWT with $\phi = 0°$ does not experience an "overshoot", it exhibits periodic oscillations in its torque profile as shown in Figure 7b. It also elucidates the reason for the VAWT not undergoing any rapid acceleration and maintaining a very low steady-state value of λ.

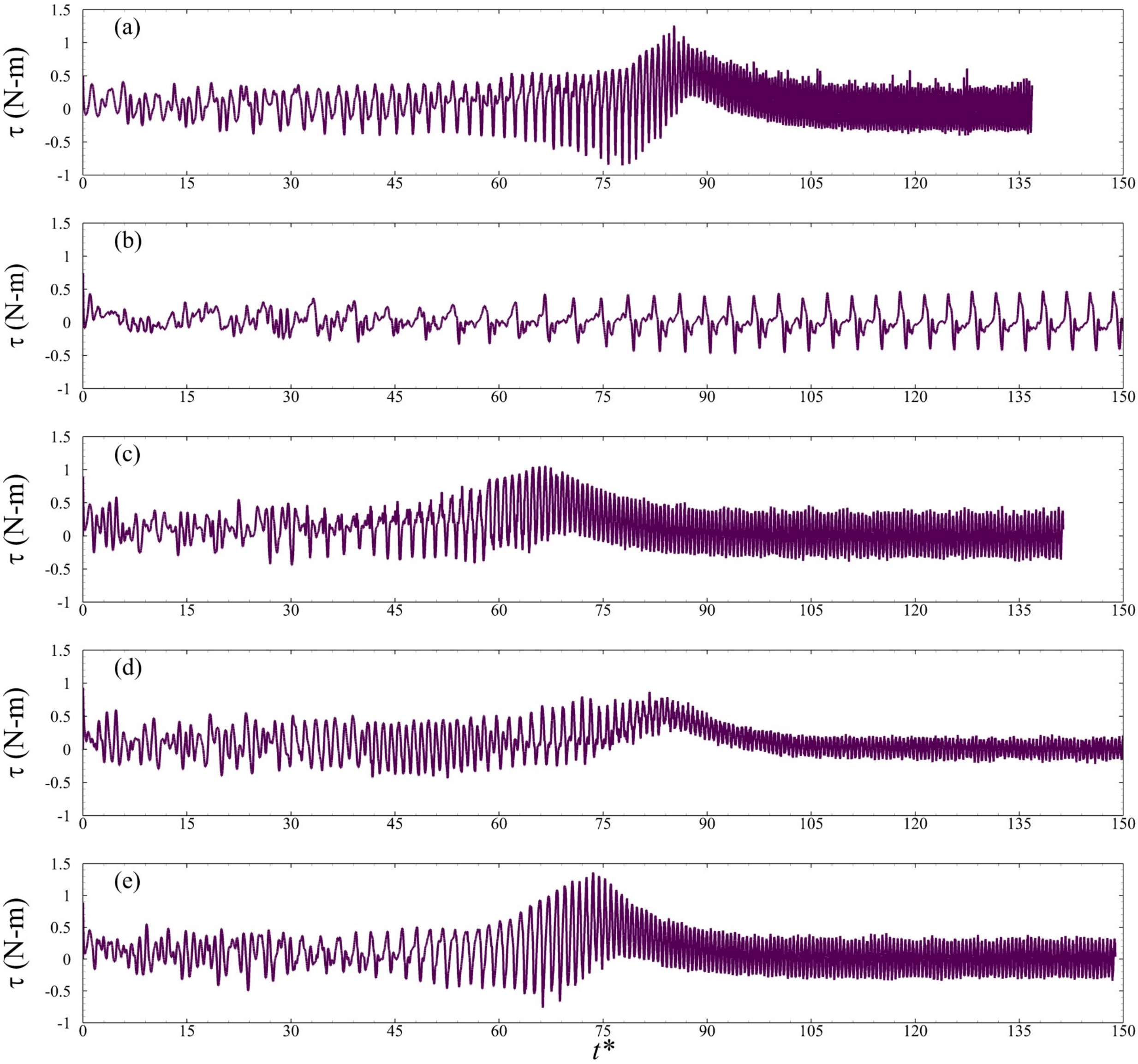

Figure 7. Variations in τ for the (**a**) single-stage turbine and dual-stage turbines with (**b**) $\phi = 0°$; (**c**) $\phi = 30°$; (**d**) $\phi = 60°$; and (**e**) $\phi = 90°$ at $U_\infty = 4$ m/s.

The quantifiable aerodynamic performance of turbines depends on the flow physics in their vicinity and its interaction with blades. Instantaneous locations of blades determine their effective angles-of-attack (α_{eff}), which can be defined as:

$$\alpha_{eff} = \tan^{-1}\frac{\sin\theta}{\cos\theta + \lambda} \tag{7}$$

Figure 8 demonstrates how α_{eff} varies as a function of the azimuthal position of blades, denoted as θ. Figure 8a explains why a dual-rotor VAWT with $\phi = 0°$ does not perform well at $U_\infty = 4$ m/s. This configuration experiences very large effective angles-of-attack. The remaining VAWTs show identical sinusoidal profiles for their angles-of-attack.

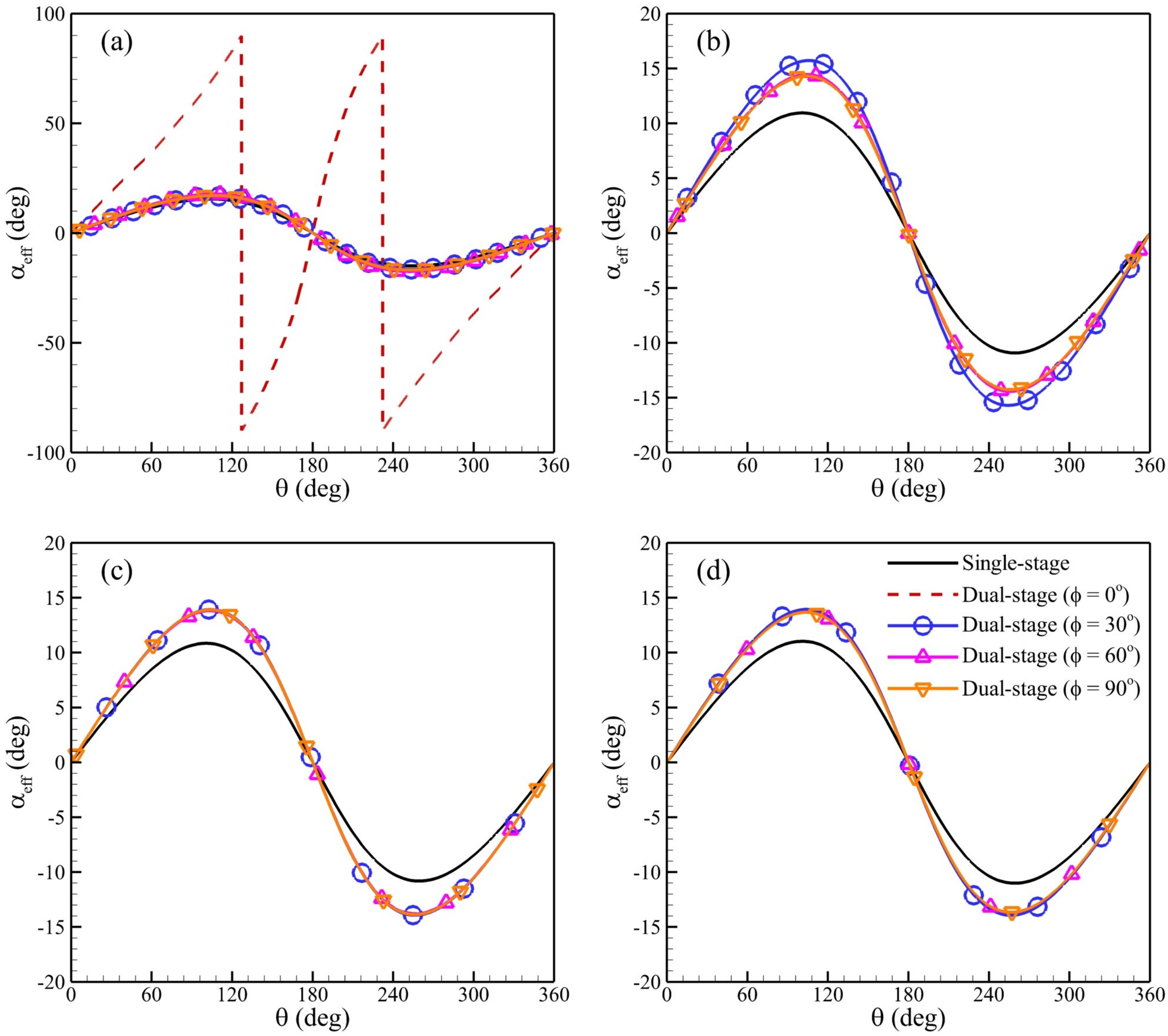

Figure 8. Variations in α_{eff} as the function of the azimuthal position (θ) of blades in the outer rotor for $U_\infty =$ (**a**) 4 m/s; (**b**) 6 m/s; (**c**) 8 m/s; and (**d**) 10 m/s.

Comparing this information with unsteady aerodynamic forces presented in Figure 9a1,a2, the large effective angles-of-attack (α_{eff}) are responsible for the production of only negative lift and lower drag over the blades of a dual-stage turbine with $\phi = 0°$. It is also noteworthy that the dual-stage VAWT with $\phi = 90°$ produces the maximum amplitudes for lift and drag at very low wind speeds. For all the remaining wind speeds in Figure 9b–d, α_{eff} remains lower than 16°. Under these flow conditions at large Reynolds numbers, dynamic stall may occur at relatively lower angles-of-attack, usually in the range of 12°–17° for NACA-0012 and NACA-0018 airfoils [45,46]. We also notice in Figure 9 that blades of the dual-stage VAWT with $\phi = 60°$ produce smaller amplitudes of unsteady lift and drag forces, which further impedes the production of greater torque.

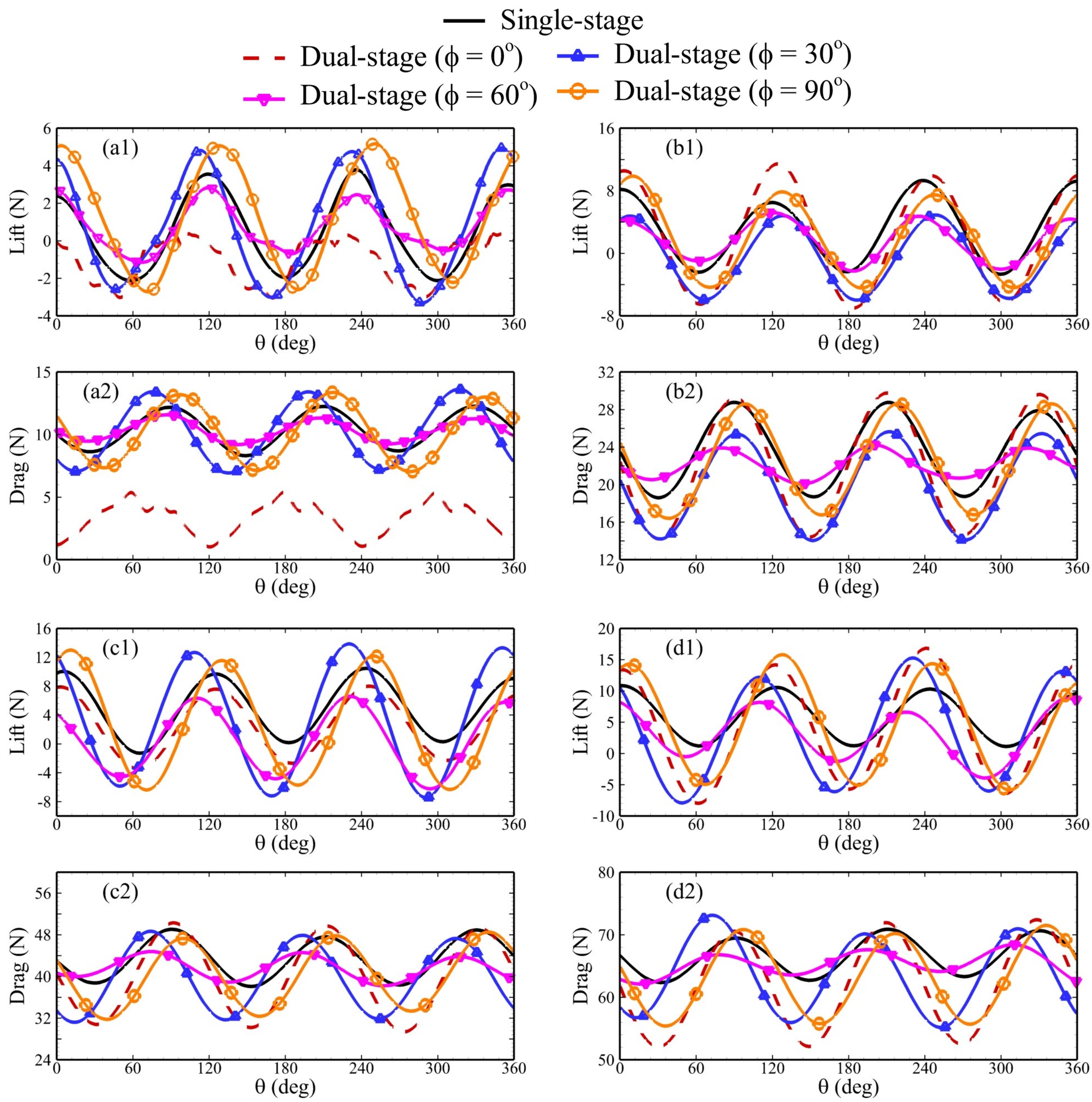

Figure 9. Variations in aerodynamic lift and drag forces versus azimuth angle (θ) for (**a1**,**a2**) $U_\infty = 4$ m/s (**b1**,**b2**) $U_\infty = 6$ m/s; (**c1**,**c2**) $U_\infty = 8$ m/s; and (**d1**,**d2**) $U_\infty = 10$ m/s.

At the end of the Introduction, it was stated that determining the power generation by dual-stage turbines should be performed only after establishing their self-starting characteristics. If they do not start faster, we believe there is no point in pursuing multi-stage rotors for VAWTs. The 6DoF starting calculations do not provide the extracted power as they only consider the flow-induced motion of rotors, whereas computations of power extraction require different solver settings to apply the equivalent of a generator load, as explained by [44]. It is important to note that other simulations, such as performed by [6], using 6DoF solvers assumed that the instantaneous torque and omega provided an equivalent metric to the steady values of power extraction, which is fundamentally wrong.

This measure may only provide the rate of work performed by the passing fluid on the blades for their rotation.

Next, we elucidate the starting process and the underlying governing flow physics for the VAWTs. When a single-stage VAWT begins rotating at $U_\infty = 4$ m/s, the blade on the windward side ($\theta = 0°$) of the flow domain produces two shear layers of opposite vorticity in the first revolution. Figure 10a illustrates this scenario. These shear layers are rolled into vortices when the blade is at $\theta > 45°$. Because the other two blades experience larger angles-of-attack at this instant, they produce large strong vortices traversing in the downstream direction. During initial revolutions of the turbine, blades start capturing vortices shed by other blades when they pass through the windward side. These interactions between blades and coherent structures cause intermittent vortex dynamics in the wake as shown in Figure 10b. Primary flow activity remains confined towards the middle of the flow domain. These flow patterns explain the production of random-looking fluctuations in temporal profiles of unsteady forces and torque. At this stage, λ remains below 0.50, while there are oscillations of low amplitudes in plots of λ (see Figure 6a). With increasing acceleration at $t^\star = 32$, the blades passing through the windward side produce distinct vortices for $\theta \sim 80°$ (see Figure 10c). It allows the blades to maintain their shear layers for a longer circumferential distance which they begin to form at $\theta = 0°$. Each following blade interacts with these shear layers, and more coherent flow structures traverse along the windward side of the wake. The vortices travelling on the leeward end of the turbines are shed from the blades passing through $180° < \theta < 270°$. Nevertheless, this flow activity expanded over the whole plane of the flow field as the turbine picks up more speed. Intense interactions of each blade with vortices and shear layers produced by the other two blades are observed in Figure 10d. We also notice the mitigation of randomness in the fluctuations of unsteady loads on blades with an increase in their amplitudes.

For $t^\star > 80$, the turbine undergoes rapid acceleration, and we see an overshoot in the torque profile (see Figure 7a). Now, the wake is clearly bounded by two vortex streets with negative and positive vortices traversing on the windward and leeward sides, respectively, as presented in Figure 10e. Vortices in the middle are not strong with smaller length scales and quickly diffuse, which means that convection of secondary coherent flow structures is suppressed by the turbine in order to reach its steady-state. The primary reason for the disappearance of flow activity from the middle of the wake is the entrapment of vortices between the rotating blades with high angular velocities on the windward side. As the turbine approaches its steady-state rotation, blades stop producing distinct vortices during their entire rotation cycle. Thus, distinct shear layers are formed and maintained, which is due to the blades experiencing angles-of-attack lower than their stall angles such that they do not undergo dynamic stall in this operational phase with increasing speed of the turbine. Stabilization of these shear layers then causes the production of helical vortices in three-dimensional flows around rotating machines [47]. In this stage of their flow-induced rotation, the shear layers of blades are only destabilized when the blades pass through the regions of entrapped vorticity on windward and leeward sides. Due to this phenomenon, more distinct coherent structures are shed on the windward side and an elongated shear layer of positive vorticity is seen to traverse in the downstream direction on the leeward side. It means that entrapment of vorticity by the rotating blades plays an important role in setting up flow dynamics in the wake to a steady-state and help the turbine attain its final λ. Although the wake is clearly asymmetric in this state, it resembles a classical von Karman vortex street behind an oscillating/rotating cylinder [48,49]. We observe similar flow phenomena for the whole range of U_∞ considered in this study. However, three important phenomena occur with increasing U_∞: (1) the region of entrapment for vortices expands between the rotating blades, (2) the vortices shed by the turbines on windward and leeward sides become stronger and bigger in size, and (3) the turbines are able to attain their steady-state operational phase in less time.

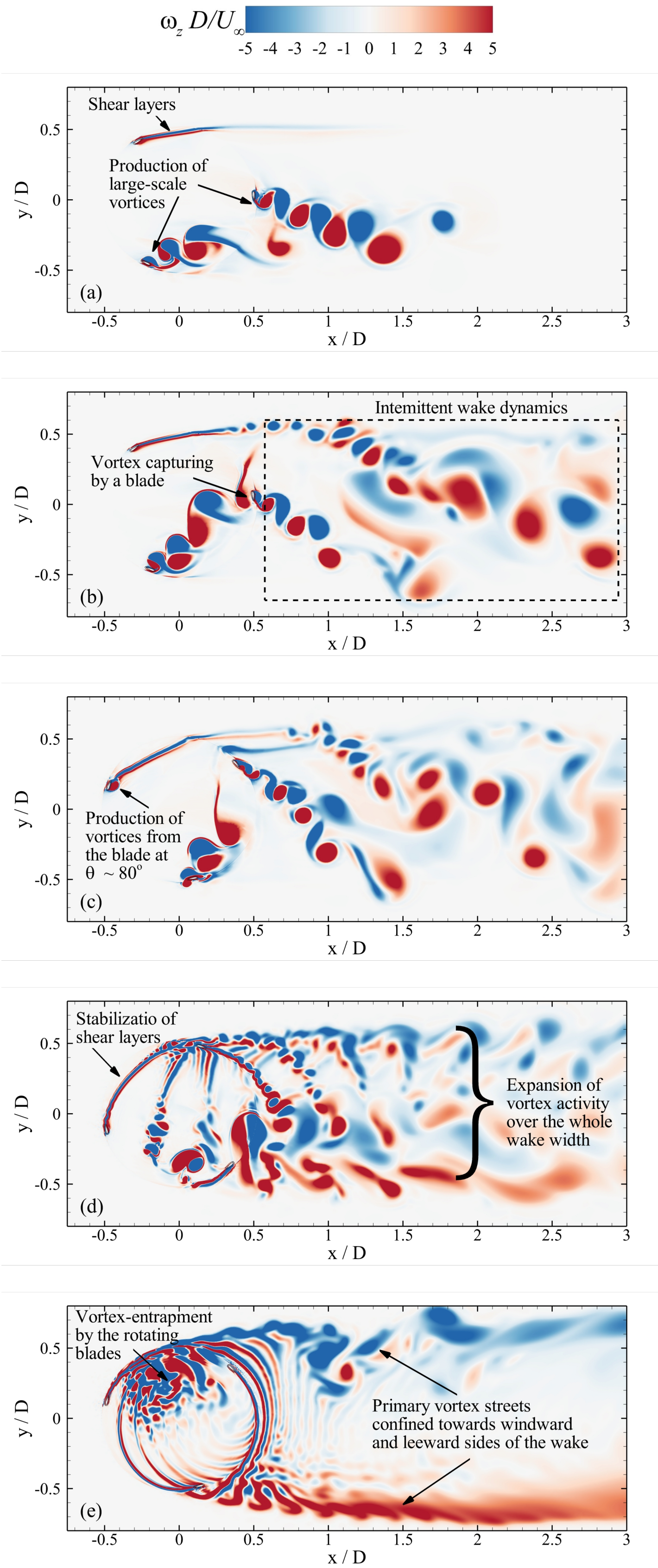

Figure 10. Vorticity contours in the flow field of a single-stage turbine at $U_\infty = 4$ m/s at (**a**) $t^\star = 6.1$; (**b**) $t^\star = 24$; (**c**) $t^\star = 32$; (**d**) $t^\star = 80.8$; and (**e**) $t^\star = 104.8$.

Similar flow physics also hold for dual-stage turbines. The readers are encouraged to watch the flow animations provided with this paper, which elucidate vorticity dynamics around the single-stage and dual-stage VAWTs for $U_\infty = 6$ m/s. Now, we describe the governing flow mechanism for the dual-stage turbine with a zero phase angle between its two stages, which appears as an exception from the abovementioned reasoning. Figure 11 explains the governing flow physics of this dual-stage VAWT. It is evident that shear layers formed in the wake of the rotating outer blades at $\theta = 0°$ are destablized due to their continuous interactions with the closely rotating inner blades. This phenomenon does not allow the blades to delay the stall process over them even after a number of rotations. Consequently, vortices are continuously formed and shed into the wake. These vortices cannot be trapped inside the rotating turbine and keep traversing in the wake. Moreover, the proximity of the inner blades and its impact on the destabilization of the shear layers could be one of the main contributing factors for the poorest starting performance of dual-stage VAWTs with $\phi = 0°$ as presented in Figure 6. Another important point here is about the dual-rotor turbines with $\phi = 60°$, reaching their steady-state rotational speeds little later than those with $\phi = 30°$ and 90°. A reasonable argument for this behavior is the stabilization of the shear layers around the rotors before their shedding in the wake. The blades arranged in tandem configurations perform better for self-starting. Their immediate presence behind their counterparts helps the turbines attain that state of stabilization. On this ground, an arrangement with $\phi = 60°$ seems to be less advantageous compared to $\phi = 30°$ and 90°.

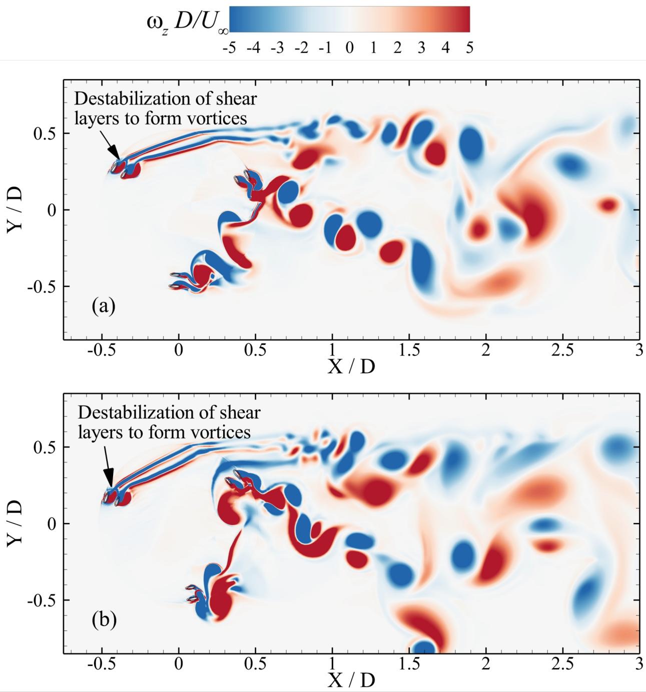

Figure 11. Vorticity contours in the flow field of a dual-stage turbine with $\phi = 0°$ at $U_\infty = 4$ m/s at (**a**) $t^\star = 47.7$ and (**b**) $t^\star = 122.5$.

4. Conclusions

In this study, numerical simulations are carried out to examine the self-starting characteristics of dual-rotor turbines in comparison to those with a single rotor. We find that, for very low wind speed of 4 m/s, dual-stage turbines with $\phi = 30°$ and 90° significantly reduce the response time to attain a steady-state tip-speed ratio, which demonstrates improvements in their self-starting process. Having $\phi = 0°$ in double-rotor turbines is not recommended because they take longer time to undergo rapid acceleration stage and reach steady-state. It experiences very large angles-of-attack during its rotation, which locks it in a dead band. Moreover, the dual-stage VAWT with $\phi = 90°$ is the best option to perform well in all wind conditions. The following three physical mechanisms play a critical role to help a turbine attain a steady angular speed: (i) stabilization of the two shear layers comprising the wake of blades passing through the windward side of a turbine, (ii) vortex-entrapment due to rotating blades and shear layers attached to them, and (iii) suppression of secondary vortex structures causing intermittent flow dynamics in the middle section of the wake of a turbine. It is important to highlight that a constant ratio of radii for the two stages are considered in our present study. Nevertheless, how variations in this important geometric parameter influence the aerodynamic performance and power generation capacity of multi-stage turbines should be the subject of a future research study.

It is also important to mention that this work ignores any load due to a generator or other drivetrain components with these VAWTs which may cause the turbine to experience large resistive moments. Their effects on the performance of dual-stage turbines are still unknown and need to be further investigated. The impact of other geometric features of blades, such as camber or chord-to-diameter ratio, should also be explored and analyzed to mitigate limitation of vertical axis wind turbines. In order to better understand the flow-induced motion of turbines and their reliance on complex vortical flow structures, three-dimensional simulations for flows around VAWTs with the addition of geometric features, such as connecting rods between the hub and blades etc., will also be carried out and reported in near future.

Author Contributions: Conceptualization, M.S.U.K. and A.H.; methodology, M.S.U.K.; software, M.S.U.K.; validation, M.S.U.K.; formal analysis, M.S.U.K., A.H. and D.W.; investigation, M.S.U.K.; writing—original draft preparation, M.S.U.K. and A.H.; writing—review and editing, M.S.U.K., A.H. and D.W.; visualization, M.S.U.K. and A.H.; funding acquisition, M.S.U.K. All authors have read and agreed to the published version of the manuscript.

Funding: This research received no external funding.

Data Availability Statement: Not applicable.

Acknowledgments: M.S.U. Khalid acknowledges the support from Natural Sciences and Engineering Research Council, Canada, through Discovery Grant.

Conflicts of Interest: The authors declare no conflict of interest.

References

1. Kirke, B.K. Evaluation of Self-Starting Vertical Axis Wind Turbines for Stand-Alone Applications. Ph.D. Thesis, Griffith University Gold Coast, Southport, Australia, 1998.
2. Lunt, P. *An Aerodynamic Model for a Vertical-Axis Wind Turbine*; MEng Project Report; School of Engineering, University of Durham: Durham, UK, 2005.
3. Takao, M.; Kuma, H.; Maeda, T.; Kamada, Y.; Oki, M.; Minoda, A. A straight-bladed vertical axis wind turbine with a directed guide vane row-Effect of guide vane geometry on the performance-. *J. Therm. Sci.* **2009**, *18*, 54–57. [CrossRef]
4. Douak, M.; Aouachria, Z.; Rabehi, R.; Allam, N. Wind energy systems: Analysis of the self-starting physics of vertical axis wind turbine. *Renew. Sustain. Energy Rev.* **2018**, *81*, 1602–1610. [CrossRef]
5. Ebert, P.; Wood, D. Observations of the starting behaviour of a small horizontal-axis wind turbine. *Renew. Energy* **1997**, *12*, 245–257. [CrossRef]
6. Celik, Y.; Ma, L.; Ingham, D.; Pourkashanian, M. Aerodynamic investigation of the start-up process of H-type vertical axis wind turbines using CFD. *J. Wind. Eng. Ind. Aerodyn.* **2020**, *204*, 104252. [CrossRef]
7. Dominy, R.; Lunt, P.; Bickerdyke, A.; Dominy, J. Self-starting capability of a Darrieus turbine. *Proc. Inst. Mech. Eng. Part A J. Power Energy* **2007**, *221*, 111–120. [CrossRef]
8. Bianchini, A.; Ferrari, L.; Magnani, S. Start-up behavior of a three-bladed H-Darrieus VAWT: Experimental and numerical analysis. *Turbo Expo Power Land Sea Air* **2011**, *54617*, 811–820.
9. Bianchini, A.; Carnevale, E.A.; Ferrari, L. A model to account for the Virtual Camber Effect in the Performance Prediction of an H-Darrieus VAWT Using the Momentum Models. *Wind. Eng.* **2011**, *35*, 465–482. [CrossRef]
10. Worasinchai, S.; Ingram, G.L.; Dominy, R.G. The physics of H-Darrieus turbine starting behavior. *J. Eng. Gas Turbines Power* **2016**, *138*, 062605. [CrossRef]
11. Batista, N.; Melício, R.; Mendes, V.; Calderón, M.; Ramiro, A. On a self-start Darrieus wind turbine: Blade design and field tests. *Renew. Sustain. Energy Rev.* **2015**, *52*, 508–522. [CrossRef]

12. Singh, M.; Biswas, A.; Misra, R. Investigation of self-starting and high rotor solidity on the performance of a three S1210 blade H-type Darrieus rotor. *Renew. Energy* **2015**, *76*, 381–387. [CrossRef]
13. Sengupta, A.; Biswas, A.; Gupta, R. Studies of some high solidity symmetrical and unsymmetrical blade H-Darrieus rotors with respect to starting characteristics, dynamic performances and flow physics in low wind streams. *Renew. Energy* **2016**, *93*, 536–547. [CrossRef]
14. Du, L.; Ingram, G.; Dominy, R.G. Experimental study of the effects of turbine solidity, blade profile, pitch angle, surface roughness, and aspect ratio on the H-Darrieus wind turbine self-starting and overall performance. *Energy Sci. Eng.* **2019**, *7*, 2421–2436. [CrossRef]
15. Sun, X.; Zhu, J.; Hanif, A.; Li, Z.; Sun, G. Effects of blade shape and its corresponding moment of inertia on self-starting and power extraction performance of the novel bowl-shaped floating straight-bladed vertical axis wind turbine. *Sustain. Energy Technol. Assess.* **2020**, *38*, 100648. [CrossRef]
16. Sun, X.; Zhu, J.; Li, Z.; Sun, G. Rotation improvement of vertical axis wind turbine by offsetting pitching angles and changing blade numbers. *Energy* **2021**, *215*, 119177. [CrossRef]
17. Mohamed, O.S.; Elbaz, A.M.; Bianchini, A. A better insight on physics involved in the self-starting of a straight-blade Darrieus wind turbine by means of two-dimensional Computational Fluid Dynamics. *J. Wind. Eng. Ind. Aerodyn.* **2021**, *218*, 104793. [CrossRef]
18. Didane, D.H.; Rosly, N.; Zulkafli, M.F.; Shamsudin, S.S. Performance evaluation of a novel vertical axis wind turbine with coaxial contra-rotating concept. *Renew. Energy* **2018**, *115*, 353–361. [CrossRef]
19. Didane, D.H.; Rosly, N.; Zulkafli, M.F.; Shamsudin, S.S. Numerical investigation of a novel contra-rotating vertical axis wind turbine. *Sustain. Energy Technol. Assess.* **2019**, *31*, 43–53. [CrossRef]
20. ZSB-AB. Doppelter Darrieus-rotor. DE202011002702U, May 2011.
21. Torabi Asr, M.; Osloob, R.; Mustapha, F. Double-Stage H-Darrieus Wind Turbine-Rotor Aerodynamics. In *Applied Mechanics and Materials*; Trans Tech Publications Ltd.: Wollerau, Switzerland, 2016; Volume 829, pp. 21–26.
22. Scungio, M.; Arpino, F.; Focanti, V.; Profili, M.; Rotondi, M. Wind tunnel testing of scaled models of a newly developed Darrieus-style vertical axis wind turbine with auxiliary straight blades. *Energy Convers. Manag.* **2016**, *130*, 60–70. [CrossRef]
23. Arpino, F.; Cortellessa, G.; Dell'Isola, M.; Scungio, M.; Focanti, V.; Profili, M.; Rotondi, M. CFD simulations of power coefficients for an innovative Darrieus style vertical axis wind turbine with auxiliary straight blades. *J. Phys. Conf. Ser.* **2017**, *923*, 012036. [CrossRef]
24. Arpino, F.; Scungio, M.; Cortellessa, G. Numerical performance assessment of an innovative Darrieus-style vertical axis wind turbine with auxiliary straight blades. *Energy Convers. Manag.* **2018**, *171*, 769–777. [CrossRef]
25. Arpino, F.; Cortellessa, G.; Massarotti, N.; Mauro, A.; Scungio, M. Numerical performance assessment of a novel Darrieus-style VAWT with auxiliary straight blades. *J. Phys. Conf. Ser.* **2020**, *1589*, 012020. [CrossRef]
26. Su, H.; Dou, B.; Qu, T.; Zeng, P.; Lei, L. Experimental investigation of a novel vertical axis wind turbine with pitching and self-starting function. *Energy Convers. Manag.* **2020**, *217*, 113012. [CrossRef]
27. Malael, I.; Dragan, V. Numerical and Experimental Efficiency Evaluation of a Counter-Rotating Vertical Axis Wind Turbine. *Eng. Technol. Appl. Sci. Res.* **2018**, *8*, 3282–3286. [CrossRef]
28. Tahani, M.; Razavi, M.; Mirhosseini, M.; Razi Astaraei, F. Unsteady aerodynamic performance of Dual-Row H-Darrieus vertical axis wind turbine. *Energy Equip. Syst.* **2020**, *8*, 55–80.
29. Chen, J.; Liu, P.; Xu, H.; Chen, L.; Yang, M.; Yang, L. A detailed investigation of a novel vertical axis Darrieus wind rotor with two sets of blades. *J. Renew. Sustain. Energy* **2017**, *9*, 013307. [CrossRef]
30. Hashem, I.; Zhu, B. Metamodeling-based parametric optimization of a bio-inspired Savonius-type hydrokinetic turbine. *Renew. Energy* **2021**, *180*, 560–576. [CrossRef]
31. Islam, M.R.; Mekhilef, S.; Saidur, R. Progress and recent trends of wind energy technology. *Renew. Sustain. Energy Rev.* **2013**, *21*, 456–468. [CrossRef]
32. Manual. ANSYS FLUENT 2020R2. In *Theory Guide*; ANSYS, Inc.: Canonsburg, PA, USA, 2020.
33. Mohamed, M.H. Aero-acoustics noise evaluation of H-rotor Darrieus wind turbines. *Energy* **2014**, *65*, 596–604. [CrossRef]
34. Siddiqui, M.S.; Durrani, N.; Akhtar, I. Quantification of the effects of geometric approximations on the performance of a vertical axis wind turbine. *Renew. Energy* **2015**, *74*, 661–670. [CrossRef]
35. Ghasemian, M.; Nejat, A. Aero-acoustics prediction of a vertical axis wind turbine using Large Eddy Simulation and acoustic analogy. *Energy* **2015**, *88*, 711–717. [CrossRef]
36. Mohamed, M.H. Reduction of the generated aero-acoustic noise of a vertical axis wind turbine using CFD (Computational Fluid Dynamics) techniques. *Energy* **2016**, *96*, 531–544. [CrossRef]
37. The, J.; Yu, H. A critical review on the simulations of wind turbine aerodynamics focusin on hybrid RANS-LES methods. *Energy* **2017**, *138*, 257–289. [CrossRef]
38. Balduzzi, F.; Bianchini, A.; Maleci, R.; Ferrara, G.; Ferrari, L. Critical issues in the CFD simulation of Darrieus wind turbines. *Renew. Energy* **2016**, *85*, 419–435. [CrossRef]
39. Rezaeiha, A.; Montazeri, H.; Blocken, B. On the accuracy of turbulence models for CFD simulations of vertical axis wind turbines. *Energy* **2019**, *180*, 838–857. [CrossRef]

40. Rezaeiha, A.; Kalkman, I.; Blocken, B. CFD simulation of a vertical axis wind turbine operating at a moderate tip speed ratio: Guidelines for minimum domain size and azimuthal increment. *Energy* **2017**, *107*, 373–385. [CrossRef]
41. Balduzzi, F.; Bianchini, A.; Ferrara, G.; Ferrari, L. Dimensionless numbers for the assessment of mesh and timestep requirements in CFD simulations of Darrieus wind turbines. *Energy* **2016**, *97*, 246–261. [CrossRef]
42. Rainbird, J. The Aerodynamic Development of a Vertical Axis Wind Turbine. Master's Thesis, University of Durham, Durham, UK, 2007.
43. Asr, M.T.; Nezhad, E.Z.; Mustapha, F.; Wiriadidjaja, S. Study on start-up characteristics of H-Darrieus vertical axis wind turbines comprising NACA 4-digit series blade airfoils. *Energy* **2016**, *112*, 528–537. [CrossRef]
44. Liu, Z.; Qu, H.; Shi, H. Numerical study on self-starting performance of Darrieus vertical axis turbine for tidal stream energy conversion. *Energies* **2016**, *9*, 789. [CrossRef]
45. Worasinchai, S.; Ingram, G.; Dominy, R. A low-Reynolds-number, high-angle-of-attack investigation of wind turbine aerofoils. *Proc. Inst. Mech. Eng. Part A J. Power Energy* **2011**, *225*, 748–763. [CrossRef]
46. Timmer, W. Two-dimensional low-Reynolds number wind tunnel results for airfoil NACA 0018. *Wind Eng.* **2008**, *32*, 525–537. [CrossRef]
47. Posa, A.; Balaras, E. Large Eddy Simulation of an isolated vertical axis wind turbine. *J. Wind. Eng. Ind. Aerodyn.* **2018**, *172*, 139–151. [CrossRef]
48. Nobari, M.; Ghazanfarian, J. A numerical investigation of fluid flow over a rotating cylinder with cross flow oscillation. *Comput. Fluids* **2009**, *38*, 2026–2036. [CrossRef]
49. Mehmood, A.; Abdelkefi, A.; Hajj, M.R.; Akhtar, I. On the onset of bifurcation and nonlinear characterization of vortex-induced vibrations under varying initial conditions. *Nonlinear Dyn.* **2020**, *99*, 575–592. [CrossRef]